COMMUNICATION

Check for updates

Lorentz force-assisted growth of romanesco-like Ni–Fe nano-cone arrays for enhanced oxygen evolution reaction at high current densities†

Hongjie Liu, Yunyi Jia, Shunhang Hua, Jingjing Weng, Lumeng Wang and Cheng Yang [ID] *

The unavoidable catalyst structure disintegration in industrial water electrolysis can lead to increased overpotential thus lowering energy efficiency. Most current studies focus on enhancing the oxygen evolution reaction (OER) rate and catalytic activity by electrodepositing catalysts with various morphologies, while few address the issue of catalyst bubble release, especially under high current densities where mass transport becomes critical. This study presents a novel approach to fabricate hierarchical Romanesco-like nickel–iron nano-cone arrays (R-NiFe NCAs) *via* Lorentz-force-assisted electrodeposition under an external magnetic field. This process introduces a high density of line defects to enhance the stability of the cone structure while enriching the surface with step edges and directing the crystal phase evolution towards more stable (111) and (220) facets. The hierarchical nano-cone array exhibits excellent wettability and efficient bubble release properties. Experimental results demonstrate that the R-NiFe NCAs achieve an overpotential of only 199 mV at 10 mA cm^{-2} and 375 mV at 100 mA cm^{-2} for OER. When integrated into an anion exchange membrane water electrolyzer (AEMWE), the system remains stable for over 600 hours at a current density of 1 A cm^{-2}. Comparative studies of different nano-cone morphologies further confirm the positive role of the Romanesco-like nano-cone with richer surface structure in improving mass transfer, wettability and bubble release.

Introduction

Alkaline water electrolysis is a pivotal pathway for achieving a hydrogen-based society and has garnered significant attention from the global scientific and industrial communities.[1–5] However, under high current densities, the catalyst structures in alkaline water electrolysis tend to degrade, significantly impairing their performance and lifespan.[6] One of the primary issues is the structural disintegration of catalysts under industrial operating conditions, which leads to increased overpotentials and reduced energy efficiency. Elevated current densities exacerbate mass transport limitations, resulting in the accumulation of gas bubbles on electrode surfaces.[7] Additionally, these bubbles impede electrolyte diffusion, introduce substantial reaction resistance, and ultimately degrade the catalytic performance. Effective gas management, therefore, is as crucial as developing high-activity catalysts for achieving high reaction rates at practical operational voltages.[8,9] Recent advances in biomimetic surfaces have provided novel insights into addressing gas release challenges in electrochemical reactions.[10,11] In industrial water splitting, where reactions often occur at high current densities, electrode surfaces generate abundant gas bubbles. In such cases, if the electrode strongly adheres to the bubbles, they tend to accumulate near the surface, impeding electrolyte diffusion and introducing substantial reaction resistance.[12] Ordered micro- or nanostructured surfaces, inspired by natural systems, exhibit excellent wettability and have shown promise in minimizing bubble adhesion and accelerating gas evolution. For instance, nano-array-based super-aerophobic electrodes establish discontinuous solid–liquid–gas triple-phase contact lines (TPCLs), which significantly reduce bubble adhesion and enhance mass transfer.[13,14] Therefore, in the anion exchange membrane water electrolysis (AEMWE) technology, which dominates the market, developing electrodes with excellent wettability, stable mass transport, and efficient hydrogen evolution under high current densities is of critical and urgent research value.[15,16] However, most existing studies focus on optimizing catalytic activity or bubble behavior independently, often neglecting the synergistic effects of structural design and external field modulation.

Over the past decades, various methods have been employed for electrocatalyst synthesis, including impregnation, colloidal, microemulsion, and sputtering methods.[17] These synthesis methods are typically multi-step processes

Institute of Materials Research, Tsinghua Shenzhen International Graduate School, Tsinghua University, Shenzhen 518055, PR China.
E-mail: yang.cheng@sz.tsinghua.edu.cn

requiring high temperatures, resulting in uncontrolled morphologies and the use of capping agents or surfactants. Moreover, traditional chemical reduction methods often introduce impurities into the deposits, which can integrate into the catalysts and reduce their catalytic activity. In this study, electrodeposition has emerged as a promising alternative. Compared to commercially available plasma-sprayed electrode technologies, electrodeposited nanostructured electrodes offer higher surface areas, better uniformity, lower production costs, and superior interfacial properties.[18–20] These features endow electrodeposited nanostructures with potential advantages in enhancing catalytic efficiency and reducing costs. However, conventional electrodeposition methods face challenges such as uneven redeposition, irregular nanoparticle distribution, and the formation of small-sized nanoparticles, which result in poor mechanical stability and limited surface area of the nanostructures.[18] For instance, the nickel nano-cones predominantly exposing (220) facets, as prepared by Lei *et al.*,[21] exhibited excellent stability during 6000 hours of operation but lacked significant activity enhancements. Additionally, prolonged electrodeposition does not increase the length or volume of nano-cones but instead causes structural collapse and tilting.[22] Thus, conventional electrodeposition alone offers limited benefits for industrial applications. If microstructures with abundant high-index facets, such as (111) and (220), and excellent wettability can be developed, performance improvements would be significant.[23,24] However, achieving this requires breaking through the traditional electrodeposition process window and exploring new experimental methodologies.

Developing a feasible strategy to construct oxygen evolution catalysts with larger surface areas and stable performance under high current densities remains a challenging pursuit. To address this issue, we propose a Lorentz-force-assisted electrodeposition approach to grow Romanesco-like nickel-iron nano-cone arrays (R-NiFe NCAs). By applying a magnetic field perpendicular to the current direction during the plating process, the Lorentz force, as described by the equation:

$$F = qv \times B \qquad (1)$$

where q is the charge of the particle, v is its velocity, and B is the magnetic field strength. Charged particles experience a Lorentz force perpendicular to their direction of motion and the magnetic field, altering their trajectories and thereby influencing the growth of the electroplated layer.[25–28] Specifically, the Lorentz force reduces local ion accumulation on the electrode surface, enhancing the uniformity of the deposition layer.[29] By controlling the strength and direction of the magnetic field, the microstructure of the electroplated layer, such as grain size and orientation, can be tailored.[27,30] During the electrodeposition process, the interaction between current and magnetic field induces magnetohydrodynamic (MHD) effects, which influence the distribution and migration of ions in the electrolyte, thereby affecting the morphology and composition of the deposited layer.[30,31] While previous studies have explored the fabrication of conical nanostructures for electrocatalytic applications, the integration of hierarchical nano-cones with magnetic field-assisted growth remains largely unexplored. Utilizing the Lorentz force, we successfully fabricated multilevel Romanesco-like NiFe nano-cone arrays with enriched surface morphology through a one-step electrodeposition process. Experimental results demonstrate that an externally applied vertical magnetic field altered the deposition pathways of Ni^{2+} and Fe^{2+}, introducing secondary NiFe nano-cones atop the primary NiFe nano-cones (NiFe NCAs). This strategy not only introduces a high density of line defects to enhance the stability of the cone structures but also enriches the surface with step edges and directs the crystal phase evolution toward more stable (111) and (220) facets. The synergistic effects of the magnetic field—combining Lorentz forces and magnetic gradient forces—enable the growth of secondary nano-cones, which significantly improve mass transfer, wettability, and bubble release properties. This hierarchical design, coupled with the magnetic field-driven growth mechanism, represents a significant advancement over conventional single-level conical structures, offering enhanced performance and stability for industrial-scale water electrolysis at high current densities.

Our work demonstrates that the R-NiFe NCAs achieve an overpotential of only 199 mV at 10 mA cm^{-2} and 375 mV at 100 mA cm^{-2} for the oxygen evolution reaction (OER). When integrated into an AEMWE, the system remains stable for over 600 hours at a current density of 1 A cm^{-2}. Comparative studies of different nano-cone morphologies further confirm the positive role of the Romanesco-like nano-cones in improving mass transfer, wettability, and bubble release. By combining magnetic field modulation with hierarchical nanostructure design, this work offers a new perspective on enhancing the performance and durability of electrocatalysts for industrial water splitting. The findings not only advance the fundamental understanding of Lorentz-force-assisted electrodeposition but also provide practical insights into the development of next-generation electrodes for high-current-density applications.

Results and discussion

The fabrication process of R-NiFe NCAs is illustrated in Fig. 1. The R-NiFe NCAs were synthesized on commercial nickel foam *via* electrodeposition under an externally applied vertical magnetic field. Extended electrodeposition times were found to cause cone collapse during growth (Fig. S1†). By optimizing pH, temperature, crystal growth modifiers, reagent concentrations in the plating solution, electrodeposition time, and current density, flower-like dense nano-cones with sharp tips were successfully obtained. For comparison, nickel nano-cone arrays without Fe doping (denoted as Ni NCAs), as well as uniform NiFe nano-cone arrays without secondary cone structures (denoted as NiFe NCAs), were synthesized using identical procedures but without an applied magnetic field. The three
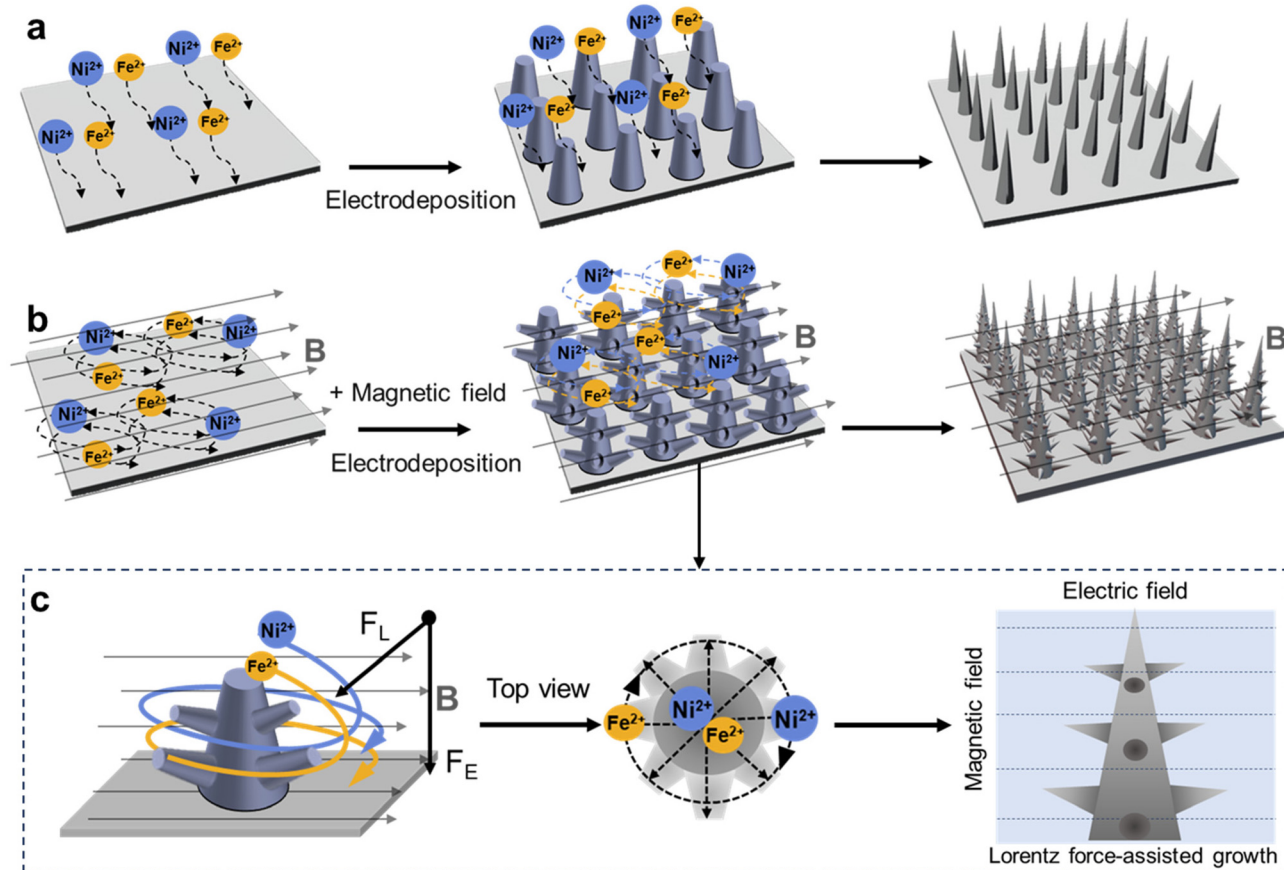
Fig. 1 Schematic illustration for the mechanism of nickel-iron nano-cone deposition on nickel foam under the influence of an external magnetic field. The electrodeposition process and morphology of nickel-iron nano-cones (a) without external magnetic field and (b) under an applied 300 Gs vertical magnetic field. (c) The role of Lorentz force in the electrodeposition of nickel-iron nano-cones under an applied vertical magnetic field. The experimental conditions for the electrodeposition were as follows: pH of 4.0, current density of 20 mA cm^{-2}, and a duration of 15 minutes. The specific material ratios and concentrations can be found in the ESI.†

different nano-cone morphologies are shown in Fig. S2.† As illustrated in Fig. 1b and c, under the influence of the vertical magnetic field, the deposition paths of Ni^{2+} and Fe^{2+} were altered by Lorentz forces. The Lorentz force induces magneto-hydrodynamic (MHD) convection (Fig. 1c), which redistributes ions (Ni^{2+}/Fe^{2+}) near the electrode surface. This reduces concentration polarization and enables uniform growth of secondary nano-cones. While the primary nano-cone structures were deposited under the effect of the electric field, the magnetic field induced the growth of secondary nano-cone structures on the surface of the primary cones, forming a Romanesco-like structure. The magnetic field not only induces Lorentz forces to redistribute ions but also generates magnetic gradient forces due to the ferromagnetic nature of Ni/Fe. As Ni/Fe are ferromagnetic, the applied magnetic field creates localized gradients, generating a magnetic gradient force. This force aligns paramagnetic Ni^{2+}/Fe^{2+} ions along field lines, promoting vertical growth of primary cones.[32] These forces work in tandem to control the growth direction and morphology of the nano-cones, resulting in a more uniform and stable structure. This dual-force mechanism is particularly effective at small scales,

where magnetic gradient forces dominate and enhance the alignment of paramagnetic ions.[32]

Scanning electron microscopy (SEM) images reveal that the dense Romanesco-like NiFe nano-cones are uniformly deposited on nickel foam (Fig. 2a and b and Fig. S3†). The primary nano-cones (Fig. 2c) and secondary nano-cones (Fig. 2g) were separated *via* ultrasonication and analyzed using transmission electron microscopy (TEM). The primary nano-cones have a length and base diameter of approximately 600 nm and 300 nm, respectively, while the secondary nano-cones measure about 200 nm in length and 50 nm in base diameter. High-resolution TEM (HRTEM) images and selected area electron diffraction (SAED) patterns indicate that the lattice parameters of both types of NiFe nano-cones are close to those of nickel (JPCDS no. 04-0850) (Fig. 2d–f and h–j). However, the primary NiFe nano-cones are predominantly oriented along the (111) crystal plane, whereas the secondary NiFe nano-cones favor the (220) crystal plane.

Energy-dispersive X-ray spectroscopy (EDX) results from TEM confirm that Ni and Fe are uniformly distributed on the surfaces of both types of NiFe nano-cones (Fig. 2f and j).
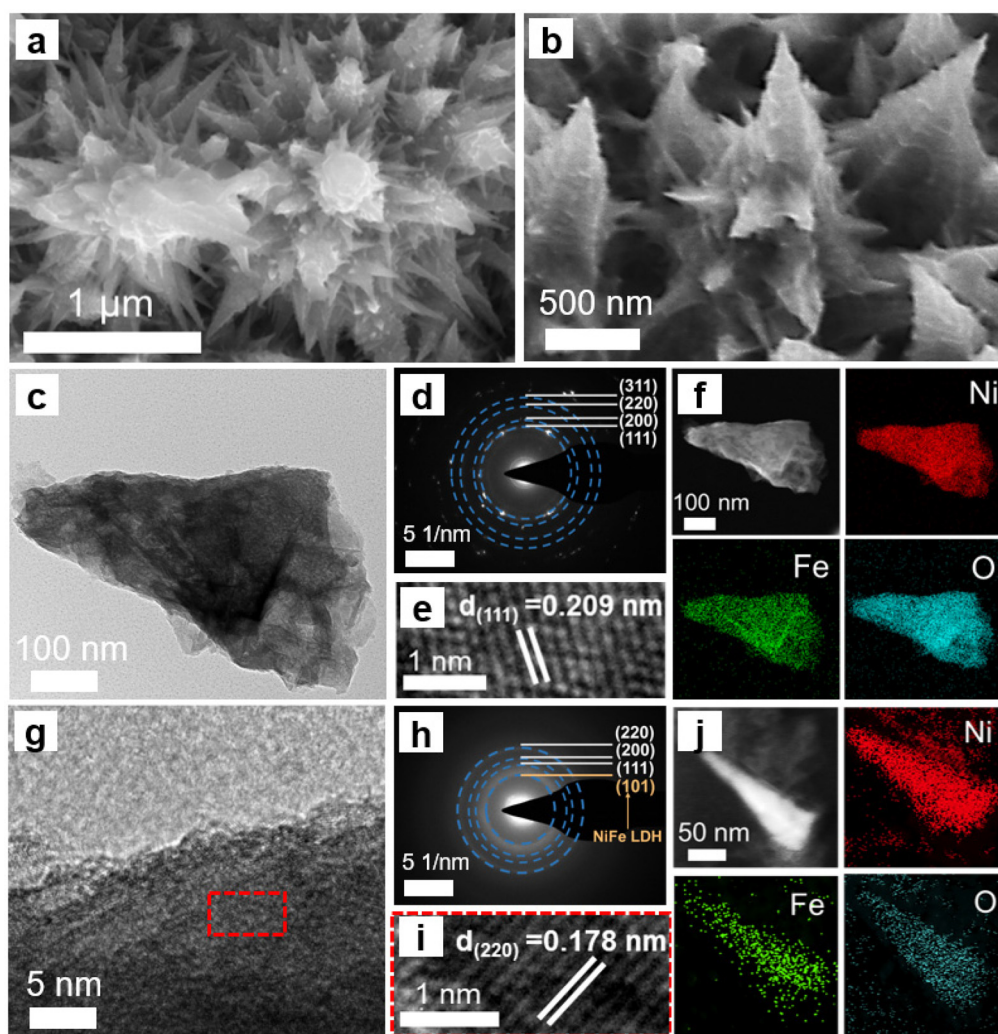
Fig. 2 (a) and (b) SEM images of R–NiFe nano-cone arrays. (c) TEM image of the primary R–NiFe nano-cones. (d) SAED pattern of the primary R–NiFe nano-cones. (e) Lattice fringes of the primary nano-cones. (f) EDX mapping images of Ni, Fe, and O elements in the primary nano-cones. (g) HRTEM image of the secondary nano-cones. (h) SAED pattern of the secondary nano-cones. (i) Magnified view of the selected area in (g). (j) EDX mapping images of Ni, Fe, and O elements in the secondary nano-cones.

Combined with the XRD spectra (Fig. 3b), these findings suggest that both types of NiFe cones are nickel-based NiFe solid-solution alloys. Additionally, the EDX spectra reveal a strong oxygen signal, attributed to the surface NiFe oxide/hydroxide layer (Fig. 2f and j).

Due to the difficulty in distinguishing signals from the nickel foam substrate (NF) and the deposited NiFe layer, R-NiFe NCAs prepared under an applied vertical magnetic field and NiFe NCAs prepared without a magnetic field were further deposited onto nickel plates. The deposited layers were then ultrasonically separated for XRD characterization. As shown in Fig. 3a, the main diffraction peaks of both materials appear at the (111), (200), and (220) crystal planes, with minimal differences in lattice parameters between R-NiFe NCAs and NiFe NCAs. However, the diffraction peak intensity of R-NiFe NCAs is significantly lower than that of NiFe NCAs, indicating reduced crystallinity in R-NiFe NCAs. This reduction correlates

with the smaller cone size and higher density of lattice defects in R-NiFe NCAs.[33] During the electrodeposition process under an applied magnetic field, more active sites, such as grain boundaries and defects, are introduced, which are more favorable for electrocatalytic performance.[34]

To clarify the chemical composition and oxidation states of R-NiFe NCAs, X-ray photoelectron spectroscopy (XPS) and depth profiling analysis were conducted. Specifically, the wide-scan XPS spectrum of the R-NiFe NCAs sample revealed the coexistence of Ni, Fe, and O elements on the surface of the nano-cones (Fig. 3b), with the surface XPS spectral fitting details (Fig. S4†). A comparison of the high-resolution Ni 2p spectra between the activated R-NiFe NCAs and NiFe NCAs (Fig. 3c) shows two main peaks corresponding to oxidized Ni and two satellite peaks (denoted as "sat."), which can be attributed to NiO or $Ni(OH)_2$.[35] For R-NiFe NCAs, the two main peaks of oxidized Ni are located at 855.6 eV (Ni $2p_{3/2}$) and
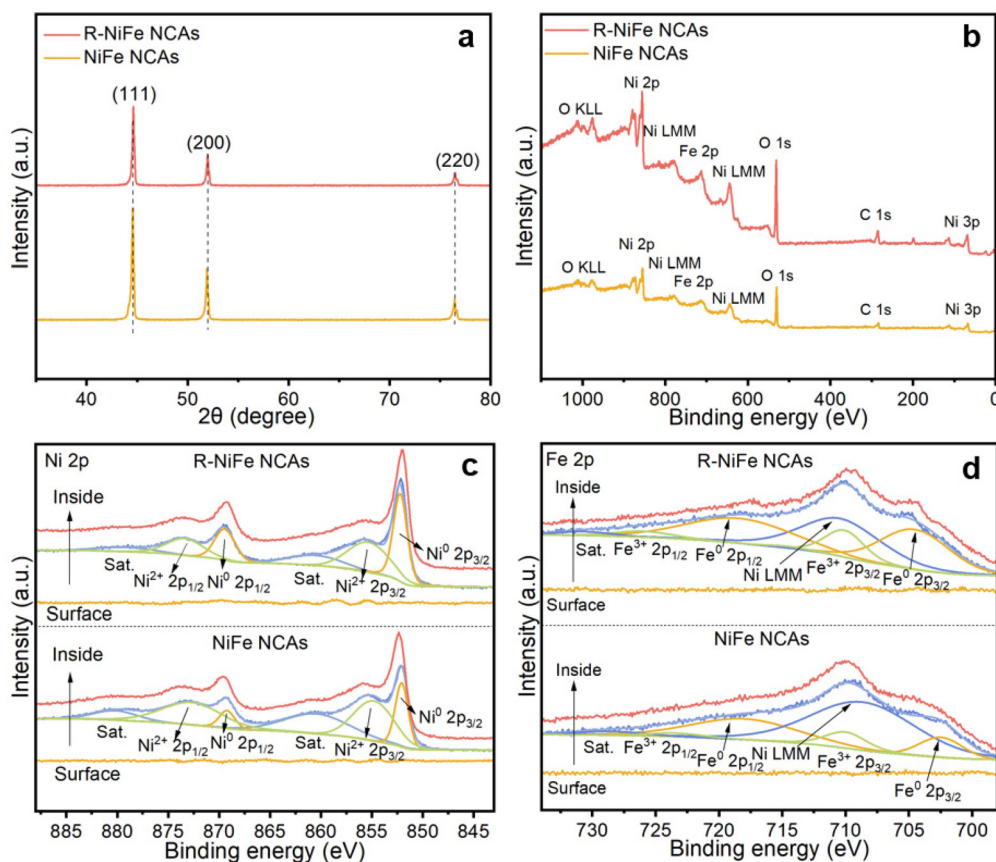
Fig. 3 Phase and composition characterization. (a) XRD patterns of the prepared NiFe and R-NiFe nano-cone arrays grown on a Ni plate substrate. (b–d) XPS analysis of NiFe and R-NiFe nano-cone arrays. (b) XPS survey spectra (surface). (c) Ni 2p, (d) Fe 2p XPS depth profiling analysis with sputtering depths of 0, 30, and 50 nm.

873.6 eV (Ni $2p_{1/2}$) spin–orbit doublets. Strong metallic Ni signals (852.3 and 869.7 eV) emerge after 30 nm argon ion sputtering, while the high-valence state signals become weaker (Fig. 3c). In contrast, the main peaks of oxidized Ni in NiFe NCAs appear at 855.0 eV (Ni $2p_{3/2}$) and 873.1 eV (Ni $2p_{1/2}$), with metallic Ni signals at 852.1 and 869.3 eV. As the sputtering depth increases, the Ni^{2+} signals gradually weaken and eventually disappear, leaving only the metallic Ni signals (Fig. 3c). The Fe 2p distribution (Fig. 3d) exhibits a similar trend, where signals of Fe^{3+} (presumably from Fe-doped $Ni(OH)_2$, abbreviated as $NiFe(OH)_2$)[36] gradually weaken, while metallic Fe signals in R-NiFe NCAs (peaks at 705.7 and 719.4 eV) and NiFe NCAs (peaks at 703.1 and 719.1 eV) increase from the activated surface to the interior.[35] The broad peak near 711.5 eV can be attributed to the Auger Ni LMM peak.[35]

The prepared electrodes were directly employed as working electrodes for OER electrocatalysis in 1 M KOH using a standard three-electrode cell. Prior to recording electrochemical data, all samples were pre-activated *via* 40 repeated CV scans to stabilize the surface (*in situ* oxidation). Polarization curves were recorded at a scan rate of 5 mV s^{-1} from high to low initial potentials to avoid signal overlap between Ni^{2+}/Ni^{3+} oxidation processes (details in ESI†). Catalysts such as NiFe NCAs

and Ni NCAs loaded on nickel foam were also tested as controls. As shown in Fig. 4a, the R-NiFe NCAs exhibited significantly enhanced catalytic activity compared to the control electrodes, especially demonstrating excellent OER performance at high current densities (above 250 mA cm^{-2}), with ultralow overpotentials of 264 and 274 mV at current densities of 500 and 1000 mA cm^{-2}, respectively. And the polarization curves for OER without iR compensation is shown in Fig. S5.† The Romanesco-like structure of the R-NiFe NCAs leads to a high density of step-edge sites and surface defects, which are crucial for enhancing the adsorption and desorption of reaction intermediates during the OER process.[37] The (111) and (220) facets exposed on the hierarchical nano-cone structure provide ideal sites for OER,[23] facilitating the transition from Ni^{2+} to Ni^{3+} oxidation states and the formation of a stable NiFe oxide/hydroxide layer that is known to be active in OER.[38,39] Moreover, the NiFe oxide/hydroxide layer formed during the electrochemical process acts as an additional active site for the OER, promoting the oxygen-oxygen bond formation that is critical in OER.[40] After the OER process, the nano-cones of R-NiFe NCAs retained their original morphology, showing good stability (Fig. S6†). Additionally, the R-NiFe NCAs achieved a low Tafel slope of 34 mV dec^{-1} over a wide range,
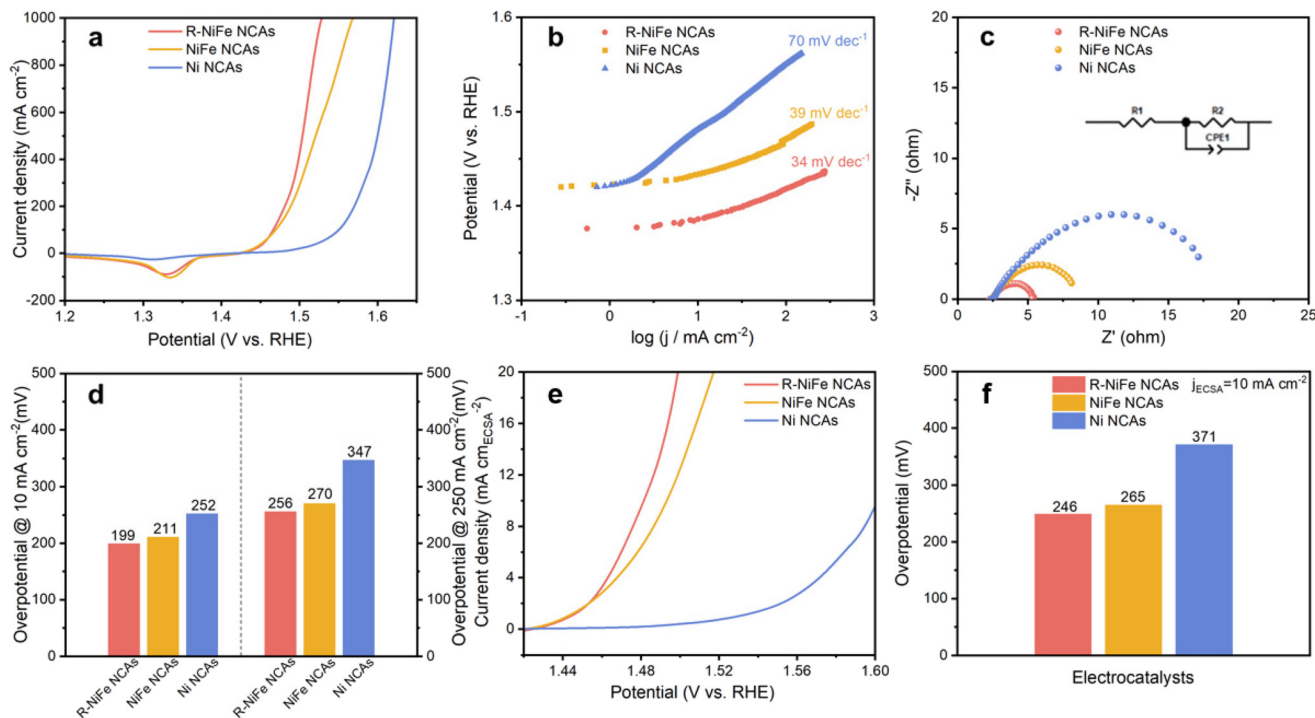
Fig. 4 Comparison of OER electrocatalytic performance of R-NiFe NCAs, NiFe NCAs, and Ni NCAs electrodes in 1 mol L^{-1} KOH solution. (a) Polarization curves based on geometric area, (b) Tafel plot, (c) EIS Nyquist plot at 300 mV OER overpotential, (d) comparison of overpotentials required to reach current densities of 10 mA cm^{-2} and 250 mA cm^{-2}, (e) polarization curves based on ECSA, (f) overpotentials required to achieve the ECSA normalized current density of 10 mA cm^{-2}. The SEM images of the catalysts described in the figure are shown in Fig. S2.†

indicating rapid OER kinetics even at high current densities (Fig. 4b). The R-NiFe NCAs exhibit a hierarchical structure that increases the electrochemically active surface area (ECSA) and facilitates more efficient charge transfer pathways. The step-rich surfaces and exposed (111) and (220) facets promote enhanced electronic conductivity and optimized adsorption/desorption of reaction intermediates, reducing charge transfer resistance. Electrochemical impedance spectroscopy (EIS) measurements further revealed that R-NiFe NCAs had the lowest charge transfer resistance (R_{ct}) among the three nanocone samples, confirming their high catalytic activity (Fig. 4c). The improved conductivity can be attributed to the high density of linear defects and the presence of multiple electron conduction pathways within the hierarchical nano-cone network. At the same overpotential, the current densities for NiFe NCAs and Ni NCAs were 350 and 660 mA cm^{-2}, and 24 and 46 mA cm^{-2}, respectively. Notably, the R-NiFe NCAs catalyst exhibited ultralow overpotentials of 199 mV and 256 mV at current densities of 10 mA cm^{-2} and 250 mA cm^{-2}, respectively, which are significantly lower than those of the other two Ni-based nano-cone OER catalysts under the same current densities (Fig. 4d). Meanwhile, the richer surface morphology and larger surface area of R-NiFe NCAs also effectively enhance the HER catalytic activity of NiFe nanocone (Fig. S7†). The active sites of R-NiFe NCAs are primarily located at the step-edge sites and defects on the surface of the nano-cones. These sites enhance the adsorption of H^{+} ions and facilitate their

reduction to hydrogen molecules. The Ni component in the NiFe alloy contributes significantly to the hydrogen adsorption and desorption processes, while the Fe atoms help in stabilizing the intermediate H* species, leading to enhanced catalytic efficiency.

The intrinsic catalytic activity of the catalysts was evaluated by normalizing the linear sweep voltammetry (LSV) curves to the electrochemically active surface area (ECSA). The ECSA values were estimated using the electrochemical capacitance method (Fig. S8†). The normalized polarization curves also demonstrated the excellent intrinsic OER catalytic activity of the R-NiFe NCAs (Fig. 4e). Specifically, the R-NiFe NCAs required an overpotential of only 246 mV to achieve a current density of 10 mA cm^{-2} (ECSA), which is lower than the 265 mV for NiFe NCAs and 371 mV for Ni NCAs (Fig. 4f).

The contact angle measurements of the R-NiFe NCAs and NiFe NCAs nano-cone electrodes (Fig. 5a and b) revealed that the contact angle of R-NiFe NCAs was only 21° (Fig. S9†), demonstrating significantly better wettability compared to NiFe NCAs. This difference is attributed to the capillary effect of the surface structure, where the capillary force generated in the flower-like nano-cone array structure adsorbs the liquid droplet onto the electrode surface. Bubble detachment was observed using a micro-camera during the OER reaction at current densities of 100 mA cm^{-2} and 250 mA cm^{-2} (Fig. 5c and d), and the statistical distribution of oxygen bubble diameters during the OER process at different current densities
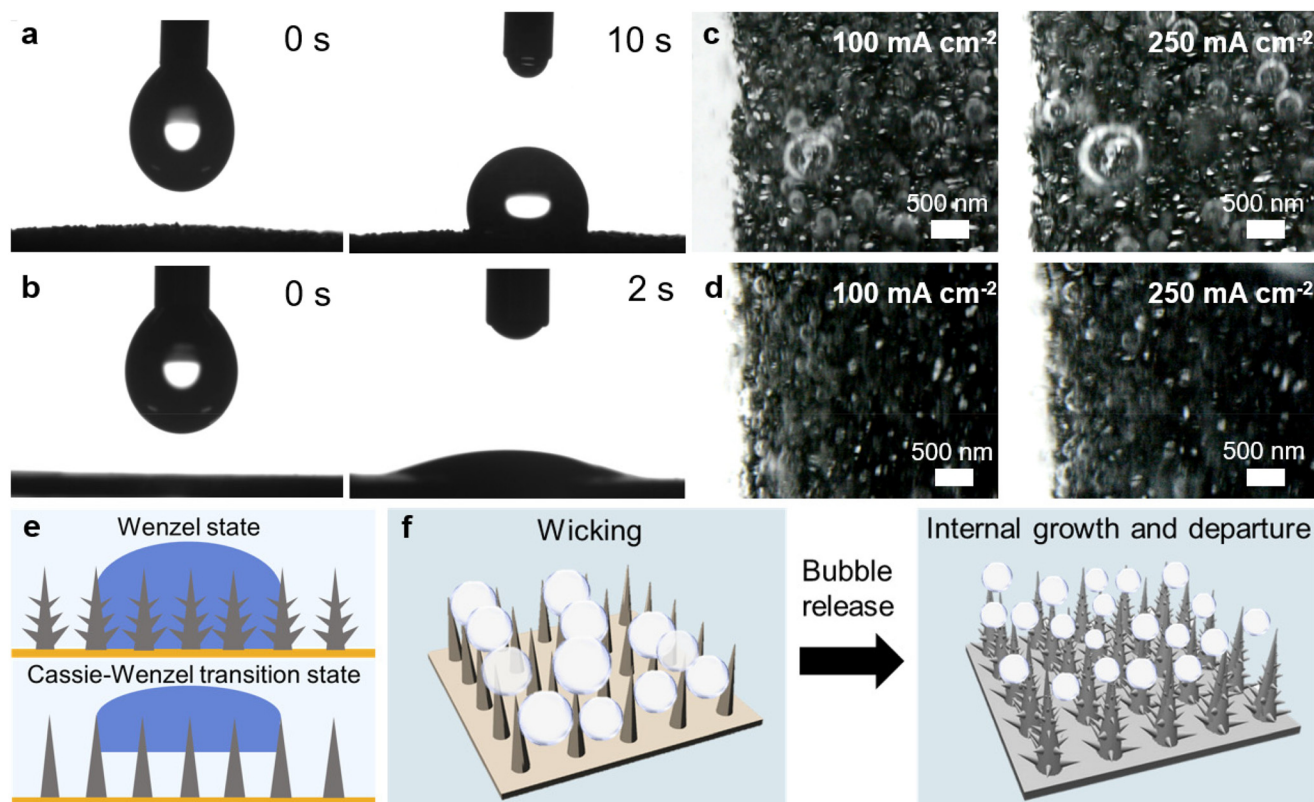
Fig. 5 Comparison of wettability and bubble release between R-NiFe NCAs and NiFe NCAs. (a) Contact angle test comparison of NiFe NCAs and (b) R-NiFe NCAs and (c) bubble imaging of NiFe NCAs and (d) R-NiFe NCAs at current densities of 100 mA cm^{-2} and 250 mA cm^{-2}, (e) schematic diagram of bubble adhesion on the surface of the two nanostructured electrode arrays, (f) schematic diagram of how the R-NiFe NCAs nanostructure promotes wettability and bubble detachment mechanisms.

was shown in Fig. S10.† The oxygen bubble detachment diameter on the R-NiFe NCAs surface was significantly smaller than that on NiFe NCAs, highlighting the excellent bubble detachment behavior of the flower-like nano-cone structure. This is crucial for water electrolysis catalysts at high current densities.[10] A wetting behavior comparison scheme (Fig. 5e) was established based on the experimental phenomena of the contact angle for two different nanoarray electrode structures. As illustrated in Fig. 5e, the multi-level nano-cone structure creates a highly rough surface, allowing the electrolyte to fully penetrate the grooves between the primary and secondary cones. This results in a discontinuous solid–liquid–gas triple-phase contact line (TPCL), where gas bubbles are fragmented into smaller sizes and detached more rapidly compared to smoother surfaces. In contrast, conventional conical electrodes often exhibit a Cassie-to-Wenzel transition, where incomplete wetting leads to gas entrapment and larger bubble adhesion.[41] Moreover, the presence of a secondary nano-cone array results in a discontinuous state for the solid–liquid–gas three-phase contact line, reducing the adhesion and separation size of gas bubbles formed on the catalyst surface.[10] The Wenzel state on R-NiFe NCAs is further supported by the extremely low contact angle of 21°, indicating strong hydrophilicity. This superwetting behavior is attributed to the capillary forces generated by

the hierarchical nano-cone array, which draws the electrolyte into the micro/nano-scale grooves. As a result, bubbles nucleate and grow within the confined spaces of the secondary cones, leading to smaller bubble sizes (<50 μm at 250 mA cm^{-2} Fig. 5d). This mechanism not only prevents bubble coalescence but also ensures continuous exposure of active sites, optimizing mass transfer and reaction kinetics at high current densities. By illustrating the bubble detachment mechanisms for the two nano-cone array structures (Fig. 5f), we can clearly observe that the multi-level nano-cone nanostructure, due to its excellent hydrophilicity and Wenzel state wettability, can reduce the release size of bubbles during the OER process. Bubble detachment becomes an internal growth and departure process,[12] preventing bubbles from growing too large and blocking active sites, thus improving mass transfer efficiency and optimizing the electrochemical process. The superwettability of R-NiFe NCAs minimizes bubble adhesion, preventing local current interruptions and ensuring continuous electrochemical reaction sites remain active. This effect, combined with the optimized charge transfer pathways, leads to lower overpotentials and improved catalytic efficiency.

To evaluate the stability of the R-NiFe NCAs in OER catalysis, we first performed 1000 CV cycles at a scan rate of 100 mV s^{-1} within the 1.2 to 1.55 V *vs.* RHE range in 1 M KOH solu-
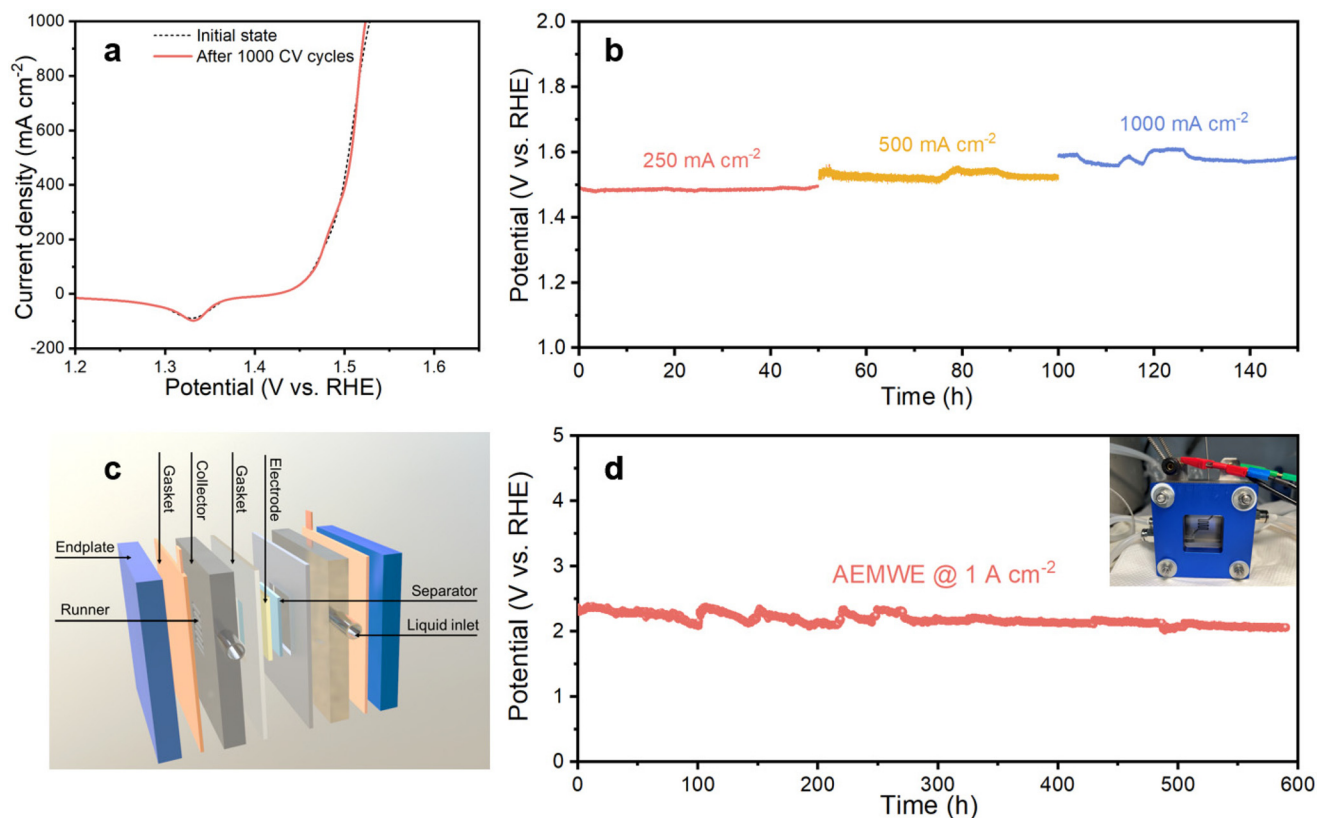
Fig. 6 Stability testing of R-NiFe NCAs catalyst electrodes. (a) Comparison of polarization curves before and after 1000 CV cycles, (b) chronopotentiometry curves at current densities of 250 mA cm^{-2}, 500 mA cm^{-2} and 1000 mA cm^{-2}, (c) schematic diagram of the AEMWE electrolyzer using R-NiFe NCAs as the anode and Ni NCAs as the cathode, (d) cell voltage $vs.$ time curve at a current density of 1 A cm^{-2} in 1 M KOH at 50 °C (without iR compensation).

tion. The LSV curves before and after testing nearly overlapped, demonstrating excellent stability (Fig. 6a). For practical applications in large-scale alkaline water electrolysis, catalysts must operate at high current densities (above 200 mA cm^{-2}) for extended periods of time.[42] Therefore, we evaluated the long-term stability of the R-NiFe NCAs catalyst using chronoamperometry, testing at 250, 500, and 1000 mA cm^{-2} for a total of 150 hours (Fig. 6b). The results showed minimal fluctuation in the real-time potential during prolonged operation, indicating the excellent durability of the R-NiFe NCAs catalyst. XRD patterns and XPS depth profiling analysis with sputtering depths of the surface nano-cone morphology (Fig. S11†) confirmed that the R-NiFe NCAs maintained their original morphology and composition after high current density OER testing.

AEMWE not only accommodates non-precious metal catalysts, such as those used in alkaline water electrolysis (AWE), but also, like proton exchange membrane water electrolysis, can produce high-purity H$_2$ (99.99%) at high current densities. Therefore, the development of advanced electrode materials for AEMWE is both practical and forward-looking.[43–45] We used R-NiFe NCAs as the anode catalyst electrode and Ni NCAs as the cathode catalyst electrode in AEMWE,[21] with a nickel foam substrate serving as the gas diffusion layer. Fig. 6c shows the AEMWE assembled structure. The stability of the AEMWE

with R-NiFe NCAs as the anode was evaluated under 50 °C, 1 M KOH (Fig. 6d). R-NiFe NCAs achieved a current density of 1 A cm^{-2} at a low cell voltage of 2.06 V in 1 M KOH. In this AEMWE system, R-NiFe NCAs exhibited excellent stability, maintaining over 600 hours of operation at a current density up to 1 A cm^{-2} with minimal changes in the required potential. This demonstrates that R-NiFe NCAs provide outstanding stability as an oxygen evolution electrode at high current densities.

Conclusions

In summary, this work demonstrates that the surface morphology of NiFe nano-cones can be effectively enriched through electrodeposition under an external magnetic field, which accelerates the alkaline OER kinetics. Experimental results show that this unique electrodeposition strategy improves the wettability of the NiFe nano-cone surface and optimizes the bubble detachment process. Compared to conventional nickel-based nano-cone electrocatalysts prepared by standard electrodeposition, the R-NiFe NCAs with monotonic nano-cone structures exhibit lower OER overpotentials, higher intrinsic OER activity, excellent wettability and efficient bubble

release properties. This study provides new insights into enhancing the stability of water electrolysis catalysts at high current densities and offer inspiration for the development of electrocatalytic system electrodes designed for gas transport processes. Given the ease and scalability of fabricating roma-nesco-like nano-cone array electrodes *via* electrodeposition, along with their excellent OER performance and long-term operational stability at high current densities (mechanical robustness), we believe this work represents a crucial step toward the industrial application of alkaline water splitting.

Data availability

All the data supporting the findings of this study are available within the article and its ESI.† Additional data related to this study is available from the corresponding author upon request.

Conflicts of interest

There are no conflicts of interest to declare.

Acknowledgements

References

1 S. A. Grigoriev, V. N. Fateev, D. G. Bessarabov and P. Millet, Current status, research trends, and challenges in water electrolysis science and technology, *Int. J. Hydrogen Energy*, 2020, **45**, 26036–26058.

2 X.-L. Liu, *et al.*, Bifunctional PdPt bimetallenes for formate oxidation-boosted water electrolysis, *Carbon Energy*, 2023, **5**, e367.

3 Z.-X. Ge, *et al.*, Interfacial engineering of holey platinum nanotubes for formic acid electrooxidation boosted water splitting, *J. Energy Chem.*, 2023, **77**, 209–216.

4 X. Zhang, *et al.*, Magnetic field-assisted microbial corrosion construction iron sulfides incorporated nickel-iron hydroxide towards efficient oxygen evolution, *Chin. J. Struct. Chem.*, 2024, **43**, 100200.

5 Y. Song, *et al.*, Coupled amorphous NiFeP/cystalline Ni3S2 nanosheets enables accelerated reaction kinetics for high current density seawater electrolysis, *Appl. Catal., B*, 2024, **352**, 124028.

6 J. Brauns and T. Turek, Alkaline Water Electrolysis Powered by Renewable Energy: A Review, *Processes*, 2020, **8**, 248.

7 H. Zhou, *et al.*, Water splitting by electrolysis at high current densities under 1.6 volts, *Energy Environ. Sci.*, 2018, **11**, 2858–2864.

8 W. Xu, Z. Lu, X. Sun, L. Jiang and X. Duan, Superwetting Electrodes for Gas-Involving Electrocatalysis, *Acc. Chem. Res.*, 2018, **51**, 1590–1598.

9 T. Kou, *et al.*, Periodic Porous 3D Electrodes Mitigate Gas Bubble Traffic during Alkaline Water Electrolysis at High Current Densities, *Adv. Energy Mater.*, 2020, **10**, 2002955.

10 M. Li, P. Xie, L. Yu, L. Luo and X. Sun, Bubble Engineering on Micro-/Nanostructured Electrodes for Water Splitting, *ACS Nano*, 2023, **17**, 23299–23316.

11 J. Wang, *et al.*, Dynamically Adaptive Bubbling for Upgrading Oxygen Evolution Reaction Using Lamellar Fern-Like Alloy Aerogel Self-Standing Electrodes, *Adv. Mater.*, 2024, **36**, 2307925.

12 R. Iwata, *et al.*, Bubble growth and departure modes on wettable/non-wettable porous foams in alkaline water splitting, *Joule*, 2021, **5**, 887–900.

13 X. Tang, *et al.*, Bioinspired Nanostructured Surfaces for On-Demand Bubble Transportation, *ACS Appl. Mater. Interfaces*, 2018, **10**, 3029–3038.

14 J. Yong, *et al.*, Bioinspired Design of Underwater Superaerophobic and Superaerophilic Surfaces by Femtosecond Laser Ablation for Anti- or Capturing Bubbles, *ACS Appl. Mater. Interfaces*, 2017, **9**, 39863–39871.

15 Y. Xu, C. Wang, Y. Huang and J. Fu, Recent advances in electrocatalysts for neutral and large-current-density water electrolysis, *Nano Energy*, 2021, **80**, 105545.

16 X.-Y. Zhang, *et al.*, Recent development on self-supported transition metal-based catalysts for water electrolysis at large current density, *Appl. Mater. Today*, 2021, **22**, 100913.

17 S. H. Ahn, I. Choi, O. J. Kwon and J. J. Kim, One-step co-electrodeposition of Pt–Ru electrocatalysts on carbon paper for direct methanol fuel cell, *Chem. Eng. J.*, 2012, **181–182**, 276–280.

18 M. B. Kale, R. A. Borse, A. Mohamed and Y. Wang, Electrocatalysts by Electrodeposition: Recent Advances, Synthesis Methods, and Applications in Energy Conversion, *Adv. Funct. Mater.*, 2021, **31**, 2101313.

19 M. Lopez and J. Ustarroz, Electrodeposition of nano-structured catalysts for electrochemical energy conversion: Current trends and innovative strategies, *Curr. Opin. Electrochem.*, 2021, **27**, 100688.

20 R. Li, *et al.*, Electrodeposition: Synthesis of advanced transition metal-based catalyst for hydrogen production via electrolysis of water, *J. Energy Chem.*, 2021, **57**, 547–566.

21 Z. Lei, *et al.*, Monolithic Nickel Catalyst Featured with High-Density Crystalline Steps for Stable Hydrogen Evolution at Large Current Density, *Small*, 2023, **19**, 2301247.

22 Y. Wang, *et al.*, Superhydrophobic Ni nanocone surface prepared by electrodeposition and its overall performance, *Surf. Coat. Technol.*, 2023, **464**, 129548.

23 P. Liu, *et al.*, Tip-Enhanced Electric Field: A New Mechanism Promoting Mass Transfer in Oxygen Evolution Reactions, *Adv. Mater.*, 2021, **33**, 2007377.

24 Z. Li, *et al.*, Alloy-strain-output induced lattice dislocation in Ni3FeN/Ni3Fe ultrathin nanosheets for highly efficient overall water splitting, *J. Mater. Chem. A*, 2021, **9**, 4036–4043.

25 Y. Yu, Z. Song, H. Ge, G. Wei and L. Jiang, Effects of Magnetic Fields on the Electrodeposition Process of Cobalt, *Int. J. Electrochem. Sci.*, 2015, **10**, 4812–4819.

26 O. Aaboubi and K. Msellak, Magnetic field effects on the electrodeposition of CoNiMo alloys, *Appl. Surf. Sci.*, 2017, **396**, 375–383.

27 J. M. D. Coey and G. Hinds, Magnetic electrodeposition, *J. Alloys Compd.*, 2001, **326**, 238–245.

28 Q. Long, Y. Zhong and J. Wu, Research Progress of Magnetic Field Techniques for Electrodeposition of Coating, *Int. J. Electrochem. Sci.*, 2020, **15**, 8026–8040.

29 Y. Huang, *et al.*, Mechanism of lithium electrodeposition in a magnetic field, *Solid State Ionics*, 2020, **345**, 115171.

30 A. Ispas, H. Matsushima, W. Plieth and A. Bund, Influence of a magnetic field on the electrodeposition of nickel–iron alloys, *Electrochim. Acta*, 2007, **52**, 2785–2795.

31 K. Kołodziejczyk, *et al.*, Influence of constant magnetic field on electrodeposition of metals, alloys, conductive polymers, and organic reactions, *J. Solid State Electrochem.*, 2018, **22**, 1629–1647.

32 L. M. A. Monzon and J. M. D. Coey, Magnetic fields in electrochemistry: The Kelvin force. A mini-review, *Electrochem. Commun.*, 2014, **42**, 42–45.

33 P. Shafi and A. Bose, Impact of crystalline defects and size on X-ray line broadening: A phenomenological approach for tetragonal SnO2 nanocrystals, *AIP Adv.*, 2015, **5**, 057137.

34 X. Geng, *et al.*, Grain boundary engineering for efficient and durable electrocatalysis, *Nat. Commun.*, 2024, **15**, 8534.

35 C. Liang, *et al.*, Exceptional performance of hierarchical Ni–Fe oxyhydroxide@NiFe alloy nanowire array electrocata-lysts for large current density water splitting, *Energy Environ. Sci.*, 2020, **13**, 86–95.

36 B. Zhang, *et al.*, High-valence metals improve oxygen evolution reaction performance by modulating 3d metal oxidation cycle energetics, *Nat. Catal.*, 2020, **3**, 985–992.

37 J. Sun, *et al.*, Synergetic Metal Defect and Surface Chemical Reconstruction into NiCo2S4/ZnS Heterojunction to Achieve Outstanding Oxygen Evolution Performance, *Angew. Chem., Int. Ed.*, 2021, **60**, 19435–19441.

38 Y.-J. Ko, *et al.*, Unraveling Ni-Fe 2D nanostructure with enhanced oxygen evolution via in situ and operando spectroscopies, *Chem. Catal.*, 2022, **2**, 2312–2327.

39 M. Gong and H. Dai, A mini review of NiFe-based materials as highly active oxygen evolution reaction electrocatalysts, *Nano Res.*, 2015, **8**, 23–39.

40 L. Trotochaud, S. L. Young, J. K. Ranney and S. W. Boettcher, Nickel–Iron Oxyhydroxide Oxygen-Evolution Electrocatalysts: The Role of Intentional and Incidental Iron Incorporation, *J. Am. Chem. Soc.*, 2014, **136**, 6744–6753.

41 S. Li, J. Huang, Z. Chen, G. Chen and Y. Lai, A review on special wettability textiles: theoretical models, fabrication technologies and multifunctional applications, *J. Mater. Chem. A*, 2017, **5**, 31–55.

42 Y. Luo, *et al.*, Morphology and surface chemistry engineering toward pH-universal catalysts for hydrogen evolution at high current density, *Nat. Commun.*, 2019, **10**, 269.

43 S.-H. Bae, *et al.*, Seamlessly Conductive 3D Nanoarchitecture of Core–Shell Ni-Co Nanowire Network for Highly Efficient Oxygen Evolution, *Adv. Energy Mater.*, 2017, **7**, 1601492.

44 J.-S. Sun, *et al.*, Nonprecious Intermetallic Al7Cu4Ni Nanocrystals Seamlessly Integrated in Freestanding Bimodal Nanoporous Copper for Efficient Hydrogen Evolution Catalysis, *Adv. Funct. Mater.*, 2018, **28**, 1706127.

45 Q. Xu, *et al.*, Anion Exchange Membrane Water Electrolyzer: Electrode Design, Lab-Scaled Testing System and Performance Evaluation, *EnergyChem*, 2022, **4**, 100087.